
CMS Physics Analysis Summary

Contact: cms-pag-conveners-susy@cern.ch

2017/03/21

Search for Supersymmetry with Higgs to diphoton decays using the razor variables at $\sqrt{s} = 13$ TeV

The CMS Collaboration

Abstract

An inclusive search for anomalous Higgs boson production in the diphoton decay channel and in association with at least one jet is presented, using the LHC proton-proton collision data collected by the CMS experiment at a center-of-mass energy of 13 TeV and corresponding to an integrated luminosity of 35.9 fb^{-1} . The razor variables M_R and R^2 as well as the momentum and mass resolution of the diphoton system are used to categorize events into different search regions. The search result is interpreted in the context of bottom squark pair production. Constraints are set on the production cross section as a function of the bottom squark and neutralino masses, and are translated into mass exclusion bounds.

1 Introduction

The discovery of the Higgs boson [1–3] at the CERN LHC has opened a new window for exploring physics beyond the standard model (SM). As the first fundamental scalar particle that can be produced and isolated in a controlled collider laboratory setting, the Higgs boson represents a new opportunity to probe physics beyond the standard model (BSM) capable of explaining the so-called hierarchy problem. Many BSM models postulate the existence of cascade decays of heavy states to Higgs bosons. In the minimal supersymmetric standard model (MSSM), Higgs bosons may be produced through the cascade decays of heavier supersymmetric particles in a variety of ways. The top and bottom squarks, supersymmetric partners of top and bottom quarks, produced via the strong interaction may decay to a Higgs boson, quarks, and the lightest supersymmetric particle (LSP), while charginos or neutralinos produced through the electroweak interaction may decay to a Higgs boson and the LSP. These examples of BSM production of Higgs bosons motivate an inclusive search for anomalous Higgs boson production that is broadly sensitive to a wide range of supersymmetric scenarios.

We present a search for supersymmetry using events with at least one Higgs boson candidate decaying to two photons, produced in association with at least one jet. The transverse momentum of the Higgs boson candidate, the expected mass resolution, and the razor variables [4, 5] M_R and R^2 , defined in Section 4 below, are used to define event categories that enhance BSM signals over SM background. Finally, the signal is extracted from the dominant non-resonant QCD background through a fit to the diphoton mass distribution. The results of the search are interpreted in a simplified model inspired by MSSM scenarios, where bottom squark pairs are produced and decay to a Higgs boson, a bottom quark, and the LSP. A diagram of this simplified model process is shown in Fig. 1.

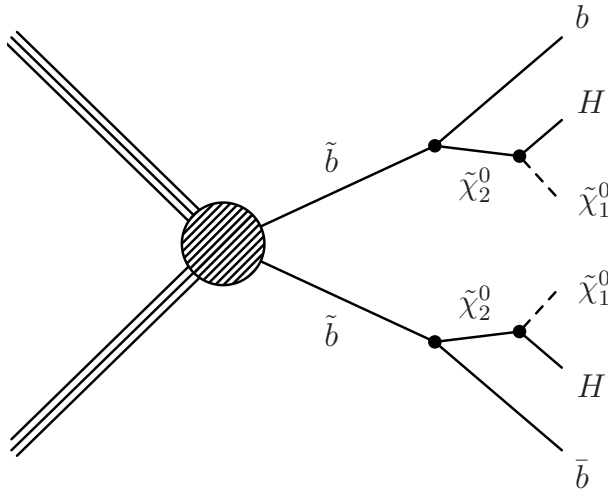


Figure 1: Diagram displaying the simplified model process for bottom squark pair production leading to Higgs bosons considered in this paper.

2 CMS Detector, Trigger, and Event Reconstruction

The central feature of the CMS detector is a superconducting solenoid of 6 m internal diameter, providing a magnetic field of 3.8 T. Within the solenoid volume are a silicon pixel and strip tracker, a lead tungstate crystal electromagnetic calorimeter (ECAL), and a brass and scintillator hadron calorimeter (HCAL), each comprising a barrel and two endcap sections. Muons are measured in gas-ionization detectors embedded in the magnet steel flux-return yoke outside the solenoid. Extensive forward calorimetry complements the coverage provided by the

barrel and endcap detectors. A more detailed description of the CMS detector, together with a definition of the coordinate system used and the relevant kinematic variables, can be found in Ref. [6].

Signal event candidates are recorded using a diphoton trigger, requiring the transverse energy of the leading and subleading photons to be larger than 30 and 18 GeV respectively, and their invariant mass to be larger than 90 GeV. Additional requirements on the shower shape and isolation are imposed to reduce the background rate and to improve the signal purity. The efficiency of the trigger with respect to events passing the offline selection was measured to be above 98%.

Physics object candidates are reconstructed using a global event description based on the CMS particle flow (PF) algorithm [7, 8], which identifies particles through an optimized combination of information from different detector systems. Photon candidates are selected by imposing additional requirements on the shower shape in the electromagnetic calorimeter, the hadronic to electromagnetic energy ratio, and the isolation in a cone around the direction of the photon momentum. The loose selection requirements were used and details may be found in reference [9]. The isolation is corrected for the effect of multiple proton collisions in a given beam crossing (pileup) by subtracting the average energy deposited into the isolation cone, estimated using a random sampling of energy density in the event. Furthermore, photon candidates are rejected if they match an electron candidate. The photon selection efficiency was measured to be about 90%. The measured energy of photons are corrected for clustering and local geometric effects using an energy regression trained on Monte Carlo simulation [9]. This regression gives a significant improvement to the energy resolution of the photons and furthermore provides an estimate of the uncertainty of the energy measurement. This uncertainty estimate is used in this search to separate events into high and low resolution categories.

Jets are clustered from PF candidates using the FASTJET [10] implementation of the anti- k_T [11] algorithm with the distance parameter $R = 0.4$. Charged PF candidates associated to a vertex other than the primary one are considered pileup and excluded. For this analysis, jets with $|\eta| < 3.0$ are considered and must not overlap with any identified photon by requiring $\Delta R = \sqrt{(\Delta\eta)^2 + (\Delta\phi)^2} > 0.5$. The combined secondary vertex (CSV) tagging algorithm [12] is used to identify jets originating from the hadronization of b quarks. A loose working point is used which yields an efficiency above 80% and a mistag rate for light flavor jets that is approximately 10%. The vector sum of the reconstructed p_T of the PF candidates is used to quantify the missing transverse momentum \vec{p}_T^{miss} in the event. Events with detector- and beam-related noise that can mimic event topologies with high energy and large $E_T^{\text{miss}} = |\vec{p}_T^{\text{miss}}|$ are filtered using dedicated noise reduction algorithms [13–15].

3 Event Simulation

Simulated Monte Carlo (MC) samples are used to model the SM Higgs backgrounds in the search regions and to calculating the selection efficiencies for SUSY signal models. Samples of SM Higgs production via gluon fusion, vector boson fusion, associated production with a W or a Z boson, $b\bar{b}H$, and $t\bar{t}H$ are generated using the next-to-leading order (NLO) MADGRAPH.aMC@NLO v2.2 [16] event generator. For the gluon fusion production mode, the sample is generated with up to two extra partons to model initial-state radiation at the matrix element level calculated at NLO accuracy. The SUSY signal samples are generated using MADGRAPH with up to two extra partons calculated at leading order accuracy. In both cases, PYTHIA v8.2 [17] is used to model the fragmentation and parton showering. The NNPDF3.0LO and NNPDF3.0NLO [18] parton distribution functions (PDF) are used with MADGRAPH and MAD-

GRAPH.aMC@NLO, respectively. The SM Higgs background samples are simulated using a GEANT4-based model [19] of the CMS detector, while the SUSY signal samples are simulated using the CMS fast simulation package [20]. All simulated events include the effects of pileup, i.e. multiple p_T collisions within the same or neighboring bunch crossings, and are processed with the same chain of reconstruction programs as is used for collision data.

The SM Higgs production cross sections are obtained from the Yellow Report 4 of the LHC Higgs Cross Section Group [21]. The SUSY signal production cross sections are calculated to next-to-leading order (NLO) plus next-to-leading-logarithm (NLL) accuracy [22–27], assuming all SUSY particles other than those in the relevant diagram to be too heavy to participate in the interaction. These NLO+NLL cross sections and their associated uncertainties [27] are used to derive the exclusion limits on the masses of the SUSY particles.

4 Event Selection and Search Categories

We select events with two photons that satisfy the selection criteria described above. Both photons must be in the barrel region of the detector, with $|\eta| < 1.4442$, and must have $p_T > 20 \text{ GeV}$. At least one of the two photons must have $p_T > 40 \text{ GeV}$. If multiple photon pairs are identified, the pair with the largest scalar sum of the transverse momenta of the photons is chosen as the Higgs candidate in the event. The Higgs candidate mass and fit range is required to be between 103 GeV and 160 GeV.

In addition to the diphoton Higgs candidate, we require at least one jet with $p_T > 30 \text{ GeV}$ and $|\eta| < 3.0$. The Higgs candidate and all identified jets are clustered into two hemispheres according to the Razor *megajet* algorithm [5], and the razor variables [4] M_R and R^2 are computed as follows:

$$M_R \equiv \sqrt{(|\vec{p}^{j_1}| + |\vec{p}^{j_2}|)^2 - (p_z^{j_1} + p_z^{j_2})^2}, \quad (1)$$

$$R^2 \equiv \left(\frac{M_T^R}{M_R} \right)^2, \quad (2)$$

where \vec{p} is the momentum of a hemisphere and p_z is its longitudinal component, and j_1 and j_2 are used to label the two hemispheres. In the definition of R^2 , the variable M_T^R is defined as:

$$M_T^R \equiv \sqrt{\frac{E_T^{\text{miss}}(p_T^{j_1} + p_T^{j_2}) - \vec{p}_T^{\text{miss}} \cdot (\vec{p}_T^{j_1} + \vec{p}_T^{j_2})}{2}}. \quad (3)$$

The razor variables M_R and R^2 provide discrimination between SUSY signal models and SM background processes with SUSY signals typically having large values of M_R and R^2 , while the SM background exhibits an exponentially falling spectrum in both variables.

The selected events are categorized into four mutually exclusive categories. An event is categorized as “HighPt” if the p_T of the selected Higgs candidate is larger than 110 GeV. Otherwise, if the event contains two b-tagged jets whose invariant mass is between 76 GeV and 106 GeV, or between 110 GeV and 140 GeV, it is categorized as “H($\gamma\gamma$)-H/Z(bb)”. The remaining events are categorized as “HighRes” and “LowRes” if the diphoton mass resolution estimate σ_M/M is smaller or larger than 0.85%, respectively. Here σ_M is computed as $1/2 \times \sqrt{(\sigma_{E,\gamma 1}/E_{\gamma 1})^2 + (\sigma_{E,\gamma 2}/E_{\gamma 2})^2}$ and σ_E is the estimated energy resolution for each photon. A graphical representation of the categorization procedure is shown in Figure 2. The “HighPt”

category isolates SUSY events producing high- p_T Higgs bosons; the “H($\gamma\gamma$)-H/Z(bb)” category isolates SUSY signals that produce two Higgs bosons or a Higgs boson and a Z boson in the final state; and the HighRes and LowRes categories further improve the discrimination between signal and background in the remaining event sample.

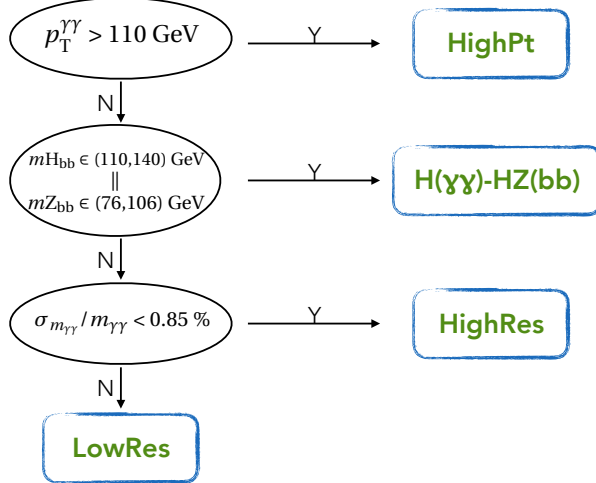


Figure 2: A flowchart showing the event categorization procedure.

Each event category is further divided into bins in the M_R and R^2 variables, which define the exclusive search regions. The definition of the search regions is summarized in Table 1. The bins defined for the HighRes and LowRes categories are kept identical to allow for simultaneous signal extraction as the relative ratio of event yields in these two categories are model-independent.

5 Background Prediction

There are two main classes of background events that pass the search selection criteria: SM Higgs production and non-resonant QCD production, with either two promptly produced photons or one prompt photon and one jet that is mistakenly identified as a photon. The SM Higgs background is estimated from the MC simulation, while the non-resonant background is predicted using a data-driven fit to the diphoton mass distribution.

Within each search bin, we extract a potential signal by performing a fit to the diphoton mass spectrum. The non-resonant background is modeled with a decaying functional form given in Table 1 for each individual search region bin. All parameters of the function are unconstrained in the fit. The functional form model for each search region bin is selected on the basis of its Akaike Information Criterion (AIC) score [28], and tests of fit biases for a set of alternative models that all describe the data in the sideband. The SM Higgs background and the SUSY signal are each modeled with a double-sided crystal ball function [29, 30] fit to the diphoton mass distribution obtained from the MC simulation. The parameters of each double-sided crystal ball function are held constant in the signal extraction fit procedure, with the exception of the parameter controlling the location of the peak which is discussed further in Section 5.1 below. The normalization of the SM Higgs background in each bin is predicted from the MC simulation, and is constrained to that value in the fit within uncertainties. Bins in the HighRes and LowRes categories are fitted simultaneously. For a given search bin, the relative yields in the HighRes and LowRes categories are observed to be largely process independent and are therefore constrained according to the simulation prediction. Based on these independent fits

Table 1: A summary of the search region bins in each category is presented. The functional form used to model the non-resonant background is also listed. An exponential function of the form e^{-ax} is denoted as “single-exp”; a linear combination of two independent exponential functions of the form e^{-ax} and e^{-bx} is denoted as “double-exp”; a modified exponential function of the form e^{-ax^b} is denoted as “mod-exp”; and a Bernstein polynomial of degree n is denoted by “poly-n”.

Bin Number	Category	M_R (GeV) Bin	R^2 Bin	Non-Resonant Bkg Model
0	HighPt	600 - ∞	0.025 - ∞	single-exp
1		150 - 600	0.130 - ∞	single-exp
2		1250 - ∞	0.000 - 0.025	single-exp
3		150 - 450	0.000 - 0.130	poly-3
4		450 - 600	0.000 - 0.035	poly-3
5		450 - 600	0.035 - 0.130	single-exp
6		600 - 1250	0.000 - 0.015	double-exp
7		600 - 1250	0.015 - 0.025	single-exp
8	H($\gamma\gamma$)-H/Z(bb)	150 - ∞	0.000 - ∞	single-exp
9	HighRes	150 - 250	0.000 - 0.175	mod-exp
10		150 - 250	0.175 - ∞	single-exp
11		250 - ∞	0.05 - ∞	single-exp
12		250 - 600	0.000 - 0.05	poly-2
13		600 - ∞	0.000 - 0.05	single-exp
9	LowRes	150 - 250	0.000 - 0.175	poly-3
10		150 - 250	0.175 - ∞	single-exp
11		250 - ∞	0.05 - ∞	poly-2
12		250 - 600	0.000 - 0.05	mod-exp
13		600 - ∞	0.000 - 0.05	single-exp

in each search bin, we obtain a model-independent search result which can be used to evaluate whether any bin exhibits statistically significant deviations from the background prediction.

We also perform a combined simultaneous fit using all search bins to try to extract specific SUSY simplified model signal hypotheses. In the combined fit, the yields for the SM Higgs background and the signal models in each bin are constrained to the MC simulation predictions within uncertainties. These uncertainties are modeled by nuisance parameters that account for various theoretical and instrumental uncertainties that can affect the SM Higgs background and SUSY signal normalization and are profiled in the fit. A more detailed discussion of systematic uncertainties can be found below in Section 5.1. The MC simulation predictions for the SM Higgs background normalization are shown in Table 2 for each search region bin.

5.1 Systematic Uncertainties

There are broadly two types of systematic uncertainties. The first and dominant systematic uncertainty is on the shape and normalization of the non-resonant background. This is propagated by profiling the normalization and shape parameters of the non-resonant background functional form in an unconstrained way. The second type of systematic uncertainty are the uncertainties on the predictions of the SM Higgs background in the various search bins. They are propagated through several independent nuisance parameters, and both theoretical and instrumental effects are taken into account. These nuisance parameters are constrained in the fit using log-normal prior functions, whose width reflects the size of the systematic uncer-

Table 2: The predicted yields for the SM Higgs background processes are shown for an integrated luminosity corresponding to 36.2 fb^{-1} for each search region considered in this analysis. The contributions from each SM Higgs process is shown separately, and the total is shown on the rightmost column along with its full uncertainty.

Bin	Category	Expected SM Higgs Yield					Total
		ggH	$t\bar{t}H$	VBF H	VH	bbH	
0	HighPt	3.40	1.40	0.49	0.78	0.02	6.1 ± 1.2
1	HighPt	1.67	0.58	0.18	1.83	0.01	4.3 ± 0.8
2	HighPt	5.13	0.64	2.52	0.17	0.04	8.5 ± 1.7
3	HighPt	55.40	0.96	10.81	6.31	0.41	73.7 ± 21.4
4	HighPt	16.90	0.50	4.71	1.14	0.18	23.4 ± 6.6
5	HighPt	3.47	0.61	0.55	0.59	0.04	5.3 ± 1.2
6	HighPt	19.35	0.80	7.57	0.82	0.15	28.6 ± 7.8
7	HighPt	5.43	0.46	1.11	0.45	0.02	7.4 ± 2.1
8	$H(\gamma\gamma)$ -H/Z(bb)	0.76	1.26	0.12	0.25	0.19	2.6 ± 0.4
9	HighRes	60.27	0.24	7.63	4.35	0.89	74.5 ± 21.8
10	HighRes	1.10	0.12	0.12	0.46	0.02	1.8 ± 0.6
11	HighRes	2.97	0.73	0.54	0.55	0.13	5.0 ± 1.4
12	HighRes	37.14	0.66	8.87	1.39	0.83	49.7 ± 14.4
13	HighRes	4.99	0.50	3.05	0.21	0.21	9.1 ± 2.7
9	LowRes	30.38	0.11	3.81	2.29	0.50	36.4 ± 10.5
10	LowRes	0.44	0.07	0.08	0.27	0.01	0.9 ± 0.2
11	LowRes	1.82	0.38	0.29	0.22	0.06	2.7 ± 0.8
12	LowRes	20.66	0.33	4.67	0.79	0.42	26.4 ± 6.4
13	LowRes	3.31	0.29	1.50	0.13	0.10	5.2 ± 1.5

tainty. They are sub-dominant as the SM Higgs background is significantly smaller than the non-resonant background. The independent effects considered include missing higher order corrections, parton distribution functions, trigger and selection efficiencies, jet energy scale uncertainties, b-tagging efficiencies, and the uncertainty on the integrated luminosity. The typical size of these effects on the expected limit is summarized in Table 3. The systematic uncertainty on the photon energy scale is implemented as a nuisance parameter that shifts the Higgs peak position, and is Gaussian constrained in the fit to lie within 1% of the nominal Higgs mass peak predicted by the MC simulation.

Table 3: Summary of systematic uncertainties and their size.

Uncertainty Source	Size
Luminosity	2.6%
PDFs and QCD Scale Variations	15-30%
Trigger and selection efficiency	3%
Jet energy scale	1-5%
Photon Energy Scale	1%
σ_M/M categorization	10 – 24%
b-tagging efficiency	4%

6 Results and Interpretations

The fit results for all search region bins are summarized in Table 4 along with the data yields, fitted background and signal yields. An example fit result for the search bin with $M_R > 600$ GeV and $R^2 > 0.025$ in the HighPt category is shown in Figure 3. Fits for all search region bins are shown in Appendix A. The observed signal significance is summarized in Figure 4 for all statistically independent search region bins. No bin exhibits a deviation from the background expectation larger than two standard deviations.

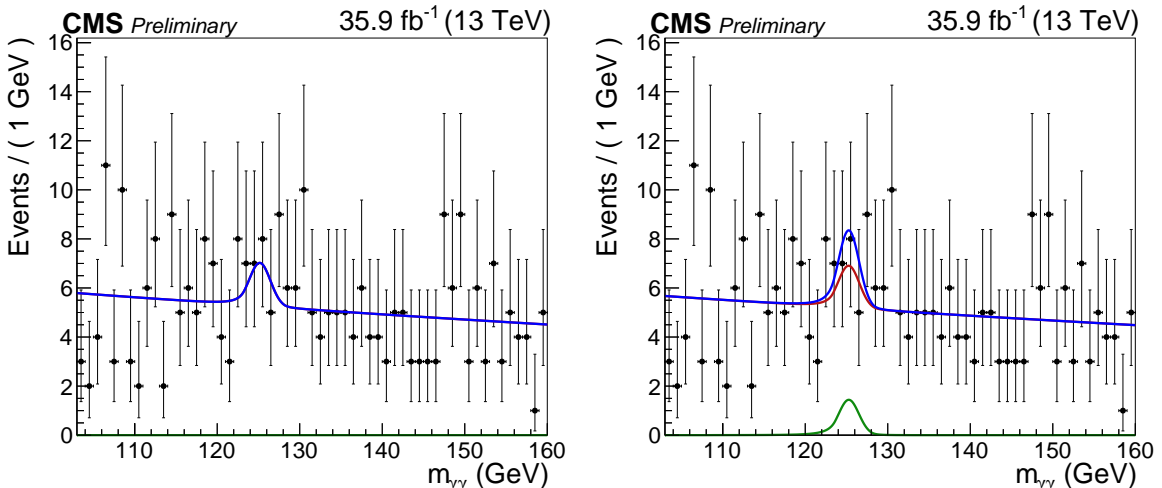


Figure 3: The diphoton mass distribution for the search region bin with $M_R > 600$ GeV and $R^2 > 0.025$ in the HighPt category are shown along with the background-only fit (left) and the signal plus background fit (right). The red curve represents the background prediction; the green curve represents the signal; and the blue curve represents the sum of the signal and background.

We interpret these search results in terms of limits on the production cross-section times branching ratio for bottom squark pair production decaying to a Higgs boson, a bottom quark and the LSP. Following the LHC-style procedure [31], we use the profile likelihood ratio test statistic and the asymptotic formula to evaluate the 95% CL observed and expected limits on the signal production cross sections that are shown in Figure 5 as a function of the bottom squark mass and the LSP mass. We exclude bottom squarks with mass below about 450 GeV for all LSP masses below 250 GeV.

Table 4: The non-resonant background yields, fitted SM Higgs background yields, best fit signal yields, and observed local significance are shown for the signal plus background fit in each search region bin. The uncertainties include both statistical and systematic components. The non-resonant background yields shown correspond to the yield within the window between 122 GeV and 129 GeV and are intended to better reflect the background under the signal peak. The observed significance for the bins in HighRes and LowRes categories are identical because they are the result of a simultaneous fit. The significance is computed using the profile likelihood, where the sign reflects whether an excess (positive sign) or deficit (negative sign) is observed.

Bin	Category	Non-Resonant Bkg	Yields	Obs. Local Significance	
			Non-Resonant Bkg	Fitted SM Higgs	Best Fit Signal
0	HighPt	36.2 ± 2.4	6.1 ± 1.2	4.8 ± 6.3	0.7σ
1	HighPt	37.2 ± 2.5	4.3 ± 0.9	-10.9 ± 7.9	-1.4σ
2	HighPt	24.2 ± 1.9	8.5 ± 1.8	-5.1 ± 5.6	-0.9σ
3	HighPt	851.7 ± 36.7	73.7 ± 21.5	13.8 ± 38.5	0.4σ
4	HighPt	164.7 ± 14.5	23.7 ± 6.8	9.6 ± 15.9	0.6σ
5	HighPt	33.8 ± 2.3	5.2 ± 1.4	11.6 ± 7.4	1.6σ
6	HighPt	127.0 ± 2.7	28.7 ± 4.2	1.1 ± 14.7	0.1σ
7	HighPt	40.0 ± 2.5	7.4 ± 2.4	-0.3 ± 7.6	-0.0σ
8	$H(\gamma\gamma)$ - $H/Z(bb)$	64.7 ± 3.1	2.6 ± 0.4	8.0 ± 8.3	1.0σ
9	HighRes	1792.0 ± 16.5	76.5 ± 24.2	-8.5 ± 44.2	-0.2σ
10	HighRes	44.0 ± 2.7	1.9 ± 0.6	0.5 ± 7.8	0.1σ
11	HighRes	126.9 ± 4.4	5.2 ± 1.4	-8.1 ± 12.3	-0.6σ
12	HighRes	1066.3 ± 19.3	51.3 ± 16.4	9.6 ± 34.0	0.2σ
13	HighRes	150.9 ± 4.6	9.5 ± 3.1	2.0 ± 10.5	0.2σ
9	LowRes	2107.8 ± 28.3	43.1 ± 16.5	-3.6 ± 18.8	-0.2σ
10	LowRes	67.6 ± 3.0	1.0 ± 0.3	0.2 ± 2.9	0.1σ
11	LowRes	158.0 ± 10.4	3.0 ± 1.2	-4.4 ± 6.6	-0.6σ
12	LowRes	1309.7 ± 13.5	29.4 ± 8.5	5.0 ± 17.7	0.2σ
13	LowRes	192.9 ± 5.1	5.8 ± 2.1	1.1 ± 5.9	0.2σ

7 Summary

A search for anomalous Higgs boson production through decays of supersymmetric particles is performed with data collected in 2016 by the CMS experiment at the CERN LHC. Proton collisions collected at a center-of-mass energy $\sqrt{s} = 13$ TeV are considered, corresponding to an integrated luminosity of about 35.9 fb^{-1} . Higgs boson candidates are reconstructed from pairs of photons in the central part of the detector. The razor variables M_R and R^2 are used to suppress SM Higgs boson production and other SM processes. The non-resonant background is estimated through a data-driven fit to the diphoton mass distribution using a functional form model selected by a combination of the AIC score and the result of a series of bias tests. The SM Higgs background is estimated using the MC simulation, with systematics on instrumental and theoretical uncertainties propagated. We interpret the results in terms of production cross-section limits on bottom squark pair production with each decaying to a Higgs boson, a b-quark, and the LSP, and exclude bottom squarks with mass below 450 GeV for LSP masses below 250 GeV.

References

[1] ATLAS Collaboration, “Observation of a new particle in the search for the Standard Model Higgs boson with the ATLAS detector at the LHC”, *Phys. Lett. B* **716** (2012) 1,

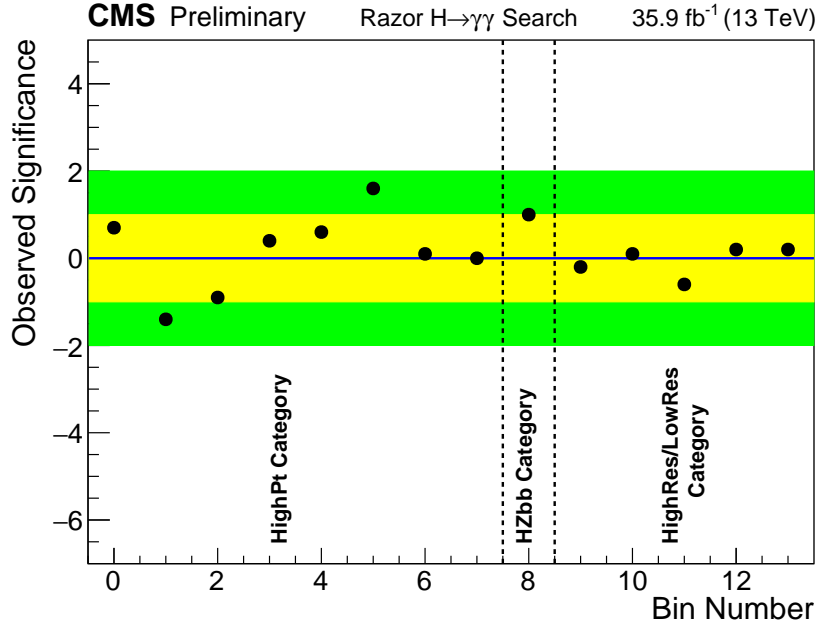


Figure 4: The observed significance in units of standard deviations is plotted for each search bin. The significance is computed using the profile likelihood, where the sign reflects whether an excess (positive sign) or deficit (negative sign) is observed. The categories that the bins belong to are labeled at the bottom. The yellow and green bands represent the 1σ and 2σ regions, respectively.

doi:10.1016/j.physletb.2012.08.020, arXiv:1207.7214.

- [2] CMS Collaboration, “Observation of a new boson at a mass of 125 GeV with the CMS experiment at the LHC”, *Phys. Lett. B* **716** (2012) 30, doi:10.1016/j.physletb.2012.08.021, arXiv:1207.7235.
- [3] CMS Collaboration, “Observation of a new boson with mass near 125 GeV in pp collisions at $\sqrt{s} = 7$ and 8 TeV”, *JHEP* **06** (2013) 081, doi:10.1007/JHEP06(2013)081, arXiv:1303.4571.
- [4] CMS Collaboration, “Inclusive search for supersymmetry using the razor variables in pp collisions at $\sqrt{s} = 7$ TeV”, *Phys. Rev. Lett.* **111** (2013) 081802, doi:10.1103/PhysRevLett.111.081802, arXiv:1212.6961.
- [5] CMS Collaboration, “Search for supersymmetry with razor variables in pp collisions at $\sqrt{s} = 7$ TeV”, *Phys. Rev. D* **90** (2014) 112001, doi:10.1103/PhysRevD.90.112001, arXiv:1405.3961.
- [6] CMS Collaboration, “The CMS experiment at the CERN LHC”, *JINST* **3** (2008) S08004, doi:10.1088/1748-0221/3/08/S08004.
- [7] CMS Collaboration, “Particle-flow event reconstruction in CMS and performance for jets, taus, and E_T^{miss} ”, CMS Physics Analysis Summary CMS-PAS-PFT-09-001, CERN, 2009.
- [8] CMS Collaboration, “Commissioning of the particle-flow event with the first LHC collisions recorded in the CMS detector”, CMS Physics Analysis Summary CMS-PAS-PFT-10-001, CERN, 2010.

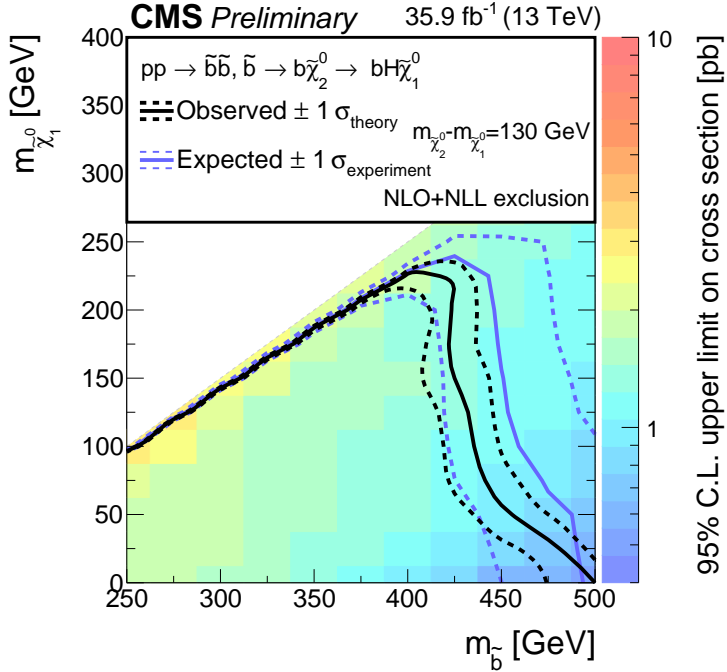


Figure 5: The observed 95% confidence level (C.L.) upper limits on the production cross section for bottom squark pair production decaying to a bottom quark, a Higgs boson, and the LSP are shown. The solid and dotted black contours represent the observed exclusion region and its 1σ bands, while the analogous blue contours represent the expected exclusion region and its 1σ bands.

- [9] CMS Collaboration, “Performance of Photon Reconstruction and Identification with the CMS Detector in Proton-Proton Collisions at $\text{sqrt}(s) = 8 \text{ TeV}$ ”, *JINST* **10** (2015), no. 08, P08010, doi:10.1088/1748-0221/10/08/P08010, arXiv:1502.02702.
- [10] M. Cacciari, G. P. Salam, and G. Soyez, “FastJet user manual”, *Eur. Phys. J. C* **72** (2012) 1896, doi:10.1140/epjc/s10052-012-1896-2, arXiv:1111.6097.
- [11] M. Cacciari, G. P. Salam, and G. Soyez, “The anti- k_t jet clustering algorithm”, *JHEP* **04** (2008) 063, doi:10.1088/1126-6708/2008/04/063, arXiv:0802.1189.
- [12] CMS Collaboration, “Identification of b quark jets at the CMS Experiment in the LHC Run 2”, CMS Physics Analysis Summary CMS-PAS-BTV-15-001, CERN, 2016.
- [13] CMS Collaboration, “Missing transverse energy performance of the CMS detector”, *JINST* **6** (2011) P09001, doi:10.1088/1748-0221/6/09/P09001, arXiv:1106.5048.
- [14] CMS Collaboration, “Search for New Physics in the Multijet and Missing Transverse Momentum Final State in Proton-Proton Collisions at $\sqrt{s} = 7 \text{ TeV}$ ”, *Phys. Rev. Lett.* **109** (2012) 171803, doi:10.1103/PhysRevLett.109.171803, arXiv:1207.1898.
- [15] CMS Collaboration, “Performance of the CMS missing transverse momentum reconstruction in pp data at $\sqrt{s} = 8 \text{ TeV}$ ”, *JINST* **10** (2015) P02006, doi:10.1088/1748-0221/10/02/P02006, arXiv:1411.0511.

[16] J. Alwall et al., “The automated computation of tree-level and next-to-leading order differential cross sections, and their matching to parton shower simulations”, *JHEP* **07** (2014) 079, doi:10.1007/JHEP07(2014)079, arXiv:1405.0301.

[17] T. Sjöstrand, S. Mrenna, and P. Skands, “A brief introduction to PYTHIA 8.1”, *Comp. Phys. Commun.* **178** (2008) 852, doi:10.1016/j.cpc.2008.01.036.

[18] NNPDF Collaboration, “Parton distributions for the LHC Run II”, *JHEP* **04** (2015) 040, doi:10.1007/JHEP04(2015)040, arXiv:1410.8849.

[19] GEANT4 Collaboration, “GEANT4—a simulation toolkit”, *Nucl. Instrum. Meth. A* **506** (2003) 250, doi:10.1016/S0168-9002(03)01368-8.

[20] CMS Collaboration, “The fast simulation of the CMS detector at LHC”, *J. Phys.: Conf. Ser.* **331** (2011) 032049, doi:10.1088/1742-6596/331/3/032049.

[21] LHC Higgs Cross Section Working Group Collaboration, “Handbook of LHC Higgs Cross Sections: 4. Deciphering the Nature of the Higgs Sector”, arXiv:1610.07922.

[22] W. Beenakker, R. Höpker, M. Spira, and P. M. Zerwas, “Squark and gluino production at hadron colliders”, *Nucl. Phys. B* **492** (1997) 51, doi:10.1016/S0550-3213(97)80027-2, arXiv:hep-ph/9610490.

[23] A. Kulesza and L. Motyka, “Threshold resummation for squark-antisquark and gluino-pair production at the LHC”, *Phys. Rev. Lett.* **102** (2009) 111802, doi:10.1103/PhysRevLett.102.111802, arXiv:0807.2405.

[24] A. Kulesza and L. Motyka, “Soft gluon resummation for the production of gluino-gluino and squark-antisquark pairs at the LHC”, *Phys. Rev. D* **80** (2009) 095004, doi:10.1103/PhysRevD.80.095004, arXiv:0905.4749.

[25] W. Beenakker et al., “Soft-gluon resummation for squark and gluino hadroproduction”, *JHEP* **12** (2009) 041, doi:10.1088/1126-6708/2009/12/041, arXiv:0909.4418.

[26] W. Beenakker et al., “Squark and gluino hadroproduction”, *Int. J. Mod. Phys. A* **26** (2011) 2637, doi:10.1142/S0217751X11053560, arXiv:1105.1110.

[27] C. Borschensky et al., “Squark and gluino production cross sections in pp collisions at $\sqrt{s} = 13, 14, 33$ and 100 TeV”, *Eur. Phys. J. C* **74** (2014) 3174, doi:10.1140/epjc/s10052-014-3174-y, arXiv:1407.5066.

[28] H. Akaike, “A new look at the statistical model identification”, *IEEE Transactions on Automatic Control* **19-6** (1974) 716–723, doi:10.1109/TAC.1974.1100705.

[29] M. Oreglia, “A Study of the Reactions $\psi' \rightarrow \gamma\gamma\psi'$ ”. PhD thesis, SLAC, 1980.

[30] J. Gaiser, “Charmonium Spectroscopy From Radiative Decays of the J/ψ and ψ'' ”. PhD thesis, SLAC, 1982.

[31] ATLAS and CMS Collaborations, “Procedure for the LHC Higgs boson search combination in summer 2011”, Technical Report ATL-PHYS-PUB-2011-011, CMS-NOTE-2011-005, CERN, 2011.

A Detailed Fit Results For All Search Region Bins

The fit results for all search bins considered are presented below in Figures 6–14.

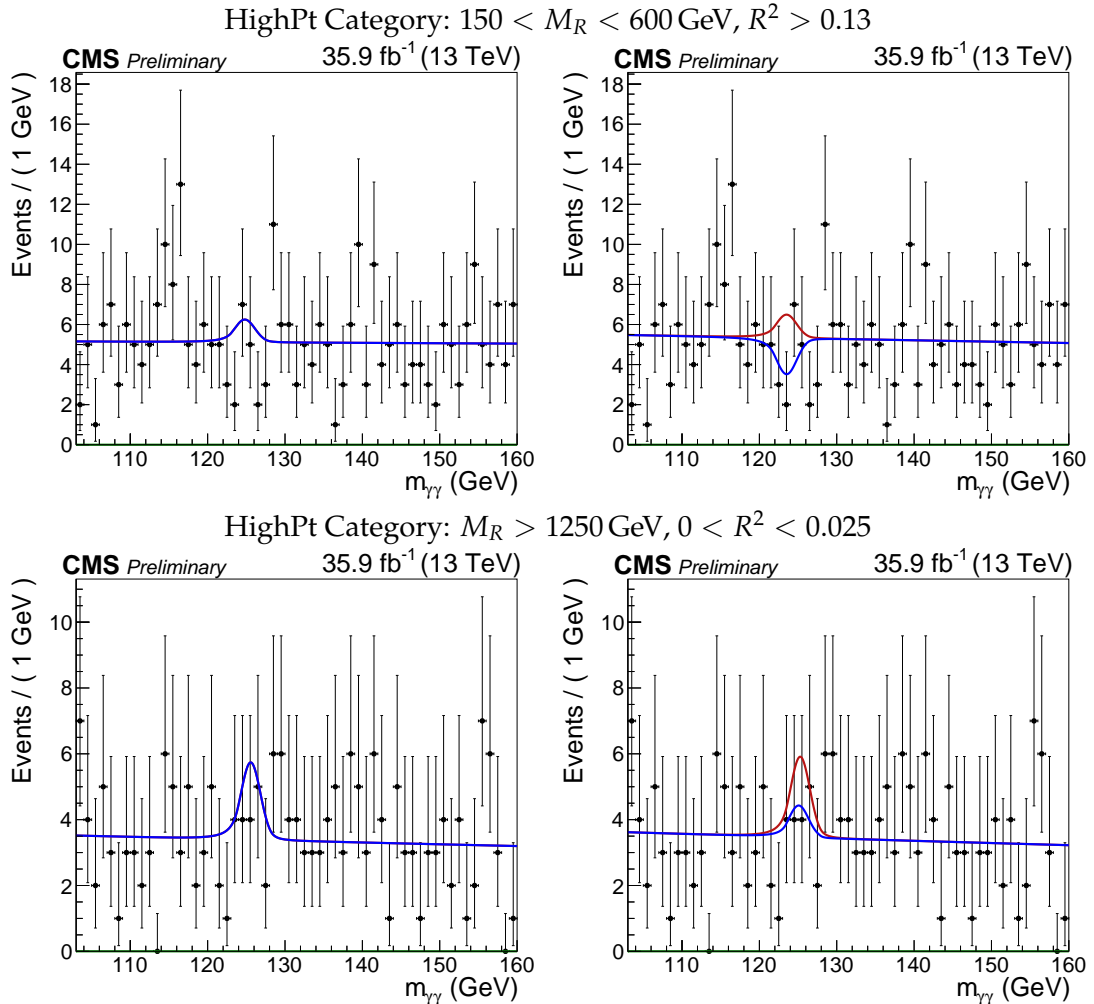


Figure 6: The diphoton mass distribution for various search region bins in the HighPt category are shown along with the background-only fit (left) and the signal plus background fit (right). The red curve represents the background prediction; the green curve represents the signal; and the blue curve represents the sum of the signal and background. The definition of the bin is labeled above each pair of plots.

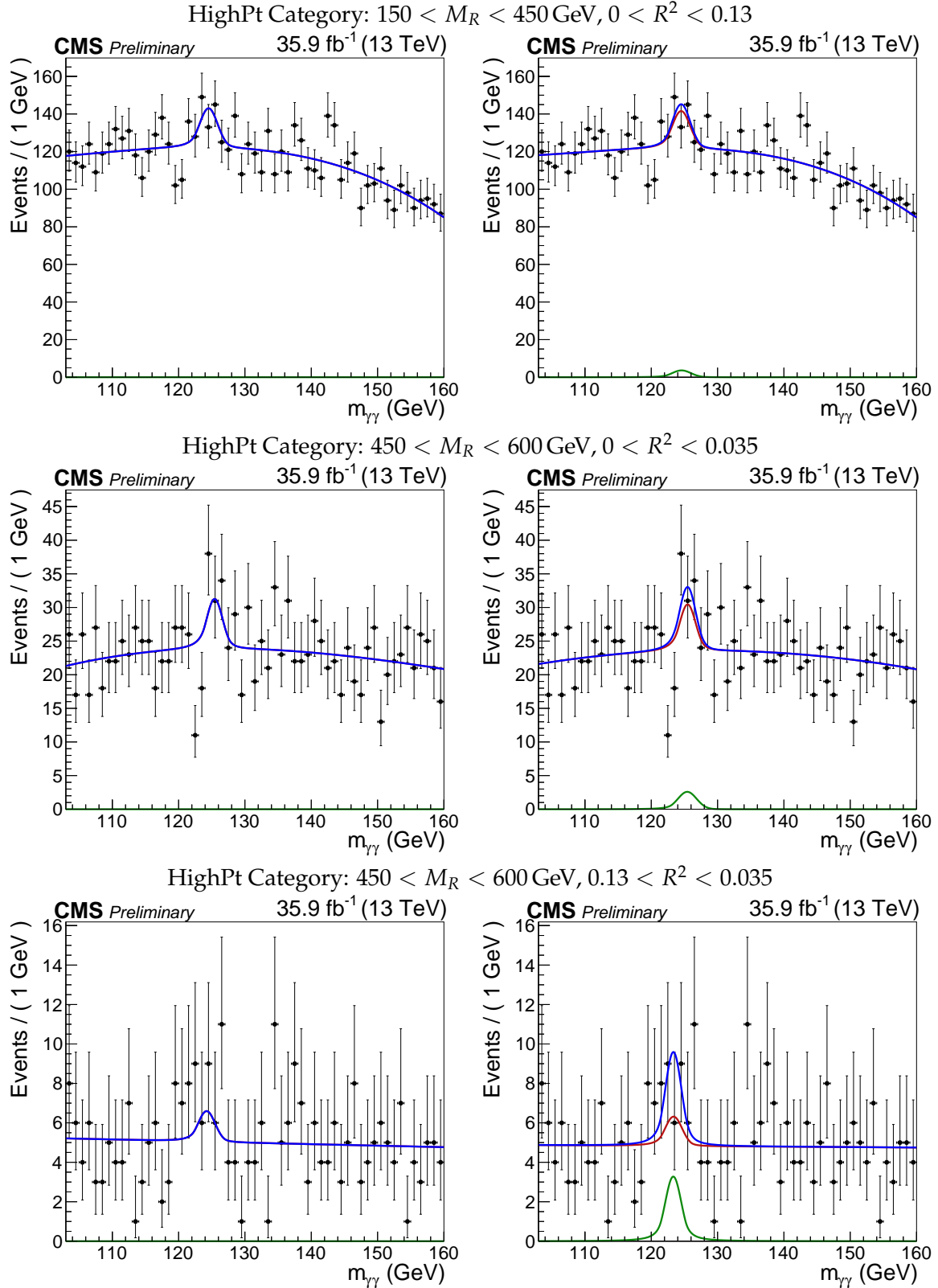


Figure 7: The diphoton mass distribution for various search region bins in the HighPt category are shown along with the background-only fit (left) and the signal plus background fit (right). The red curve represents the background prediction; the green curve represents the signal; and the blue curve represents the sum of the signal and background. The definition of the bin is labeled above each pair of plots.

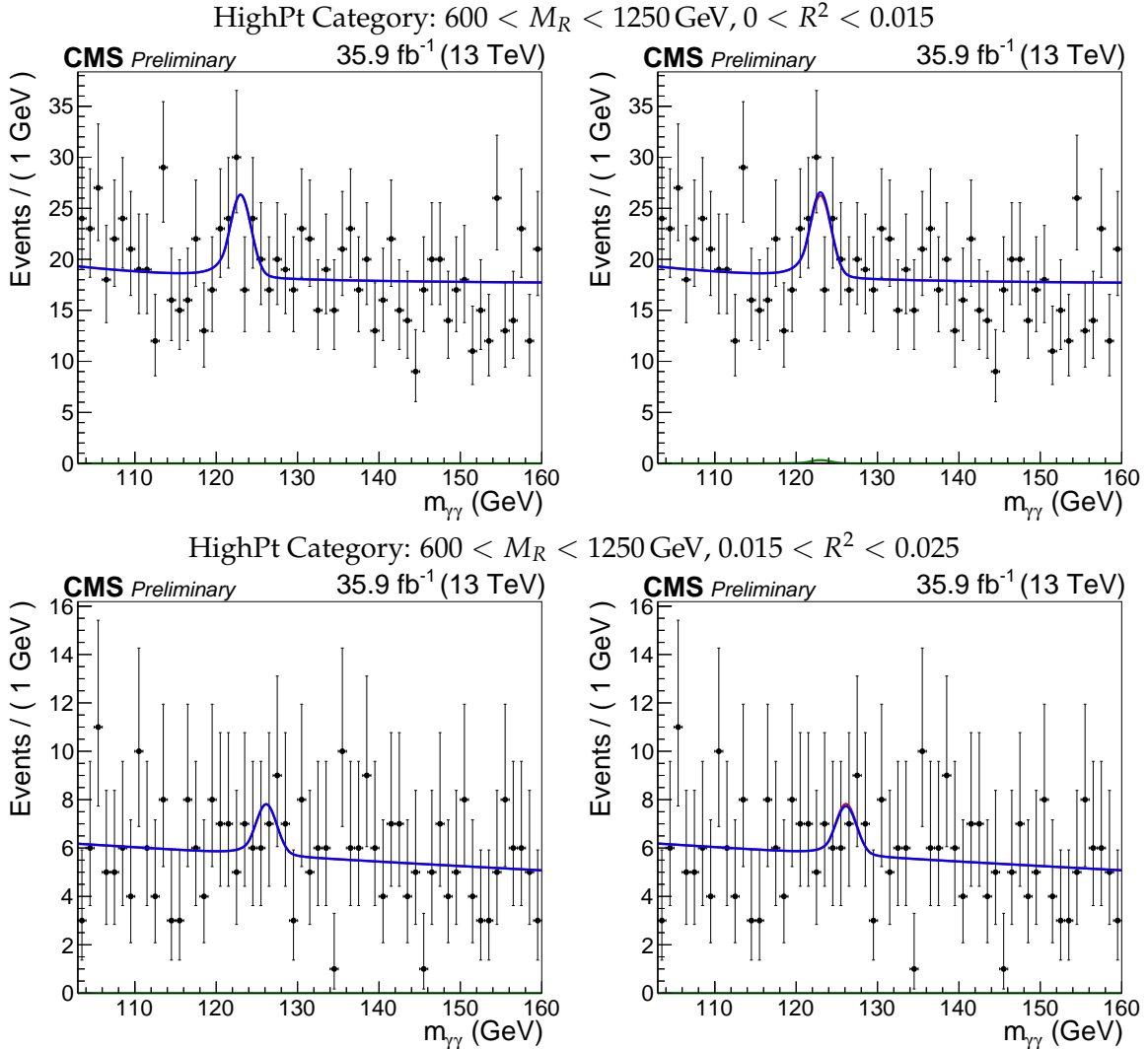


Figure 8: The diphoton mass distribution for various search region bins in the HighPt category are shown along with the background-only fit (left) and the signal plus background fit (right). The red curve represents the background prediction; the green curve represents the signal; and the blue curve represents the sum of the signal and background. The definition of the bin is labeled above each pair of plots.

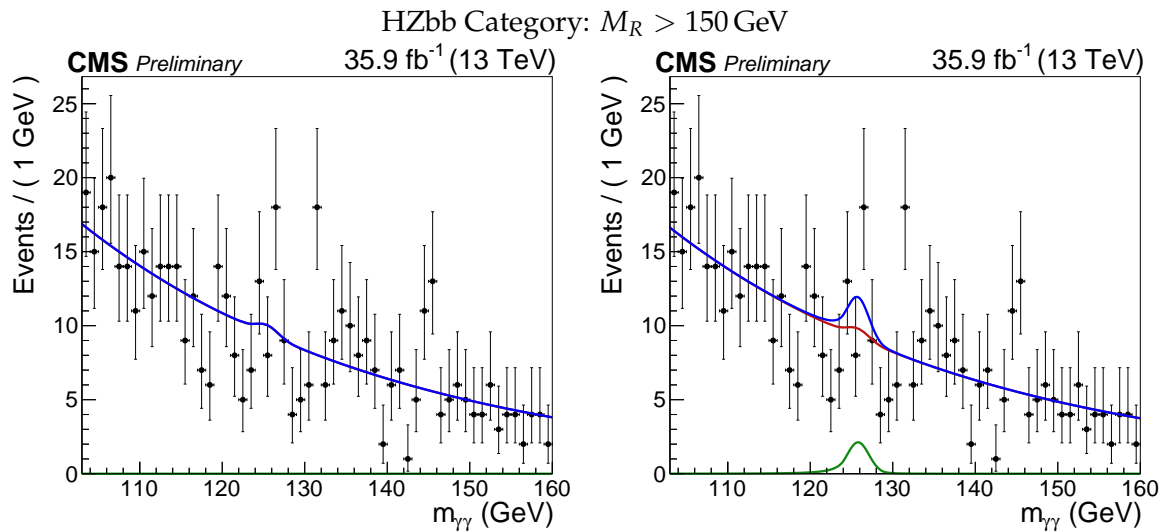


Figure 9: The diphoton mass distribution for various search region bins in the HZbb category are shown along with the background-only fit (left) and the signal plus background fit (right). The red curve represents the background prediction; the green curve represents the signal; and the blue curve represents the sum of the signal and background. The definition of the bin is labeled above each pair of plots.

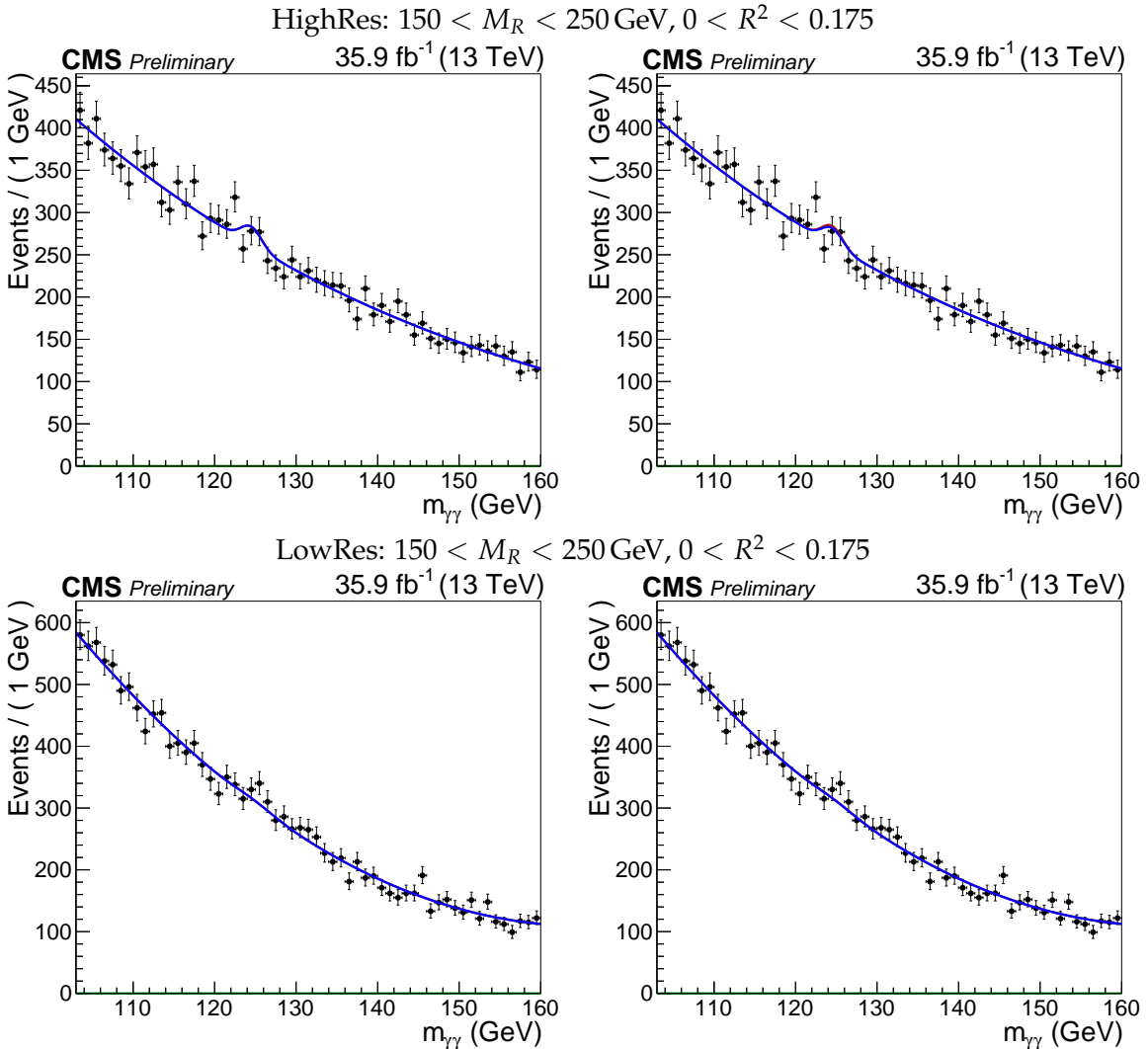


Figure 10: The diphoton mass distribution for the search region bin 9 are shown along with the background-only fit (left) and the signal plus background fit (right). The top row shows the HighRes category, while the bottom row shows the LowRes category. The red curve represents the background prediction; the green curve represents the signal; and the blue curve represents the sum of the signal and background. The definition of the bin is labeled above each pair of plots.

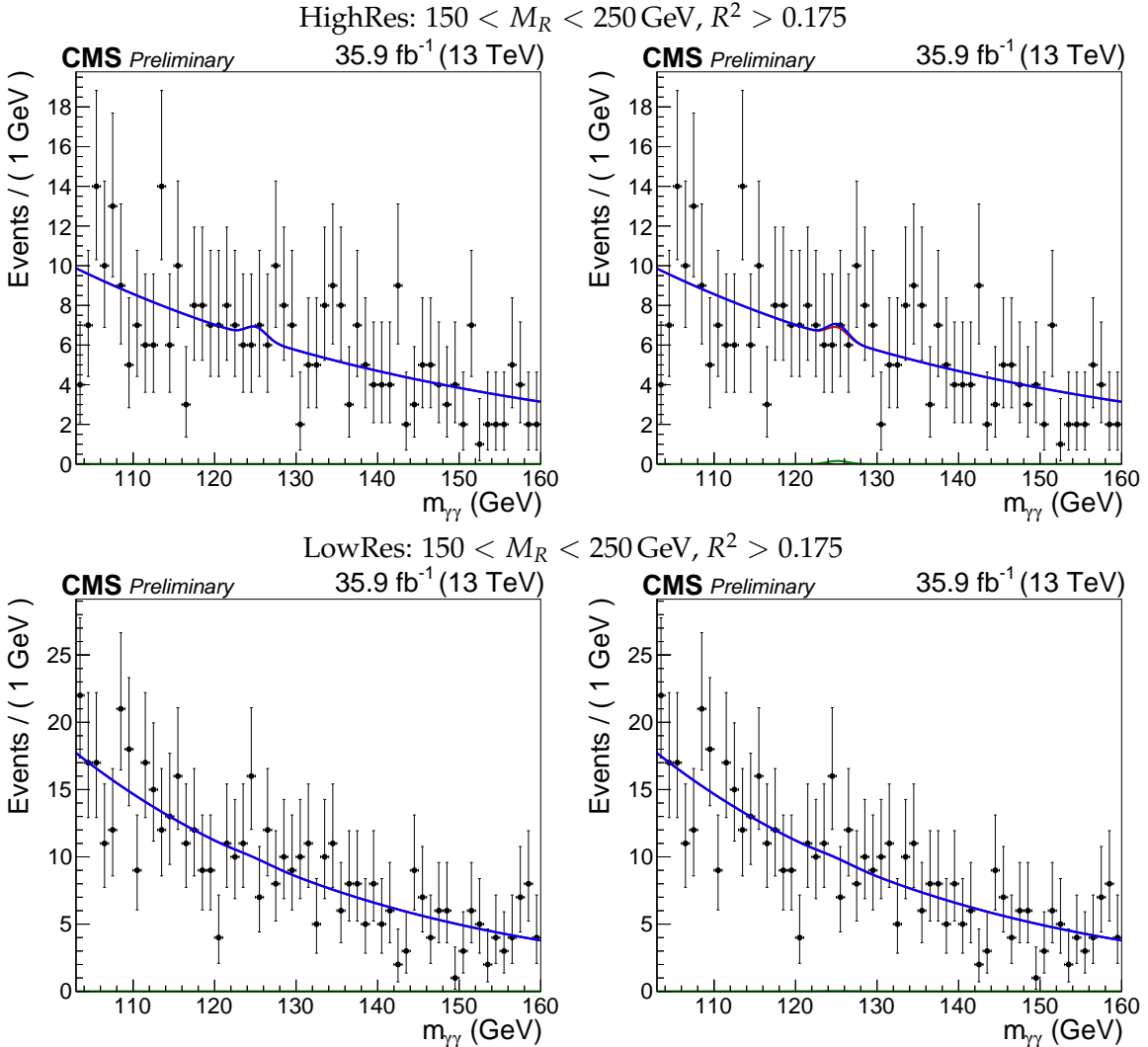


Figure 11: The diphoton mass distribution for the search region bin 10 are shown along with the background-only fit (left) and the signal plus background fit (right). The top row shows the HighRes category, while the bottom row shows the LowRes category. The red curve represents the background prediction; the green curve represents the signal; and the blue curve represents the sum of the signal and background. The definition of the bin is labeled above each pair of plots.

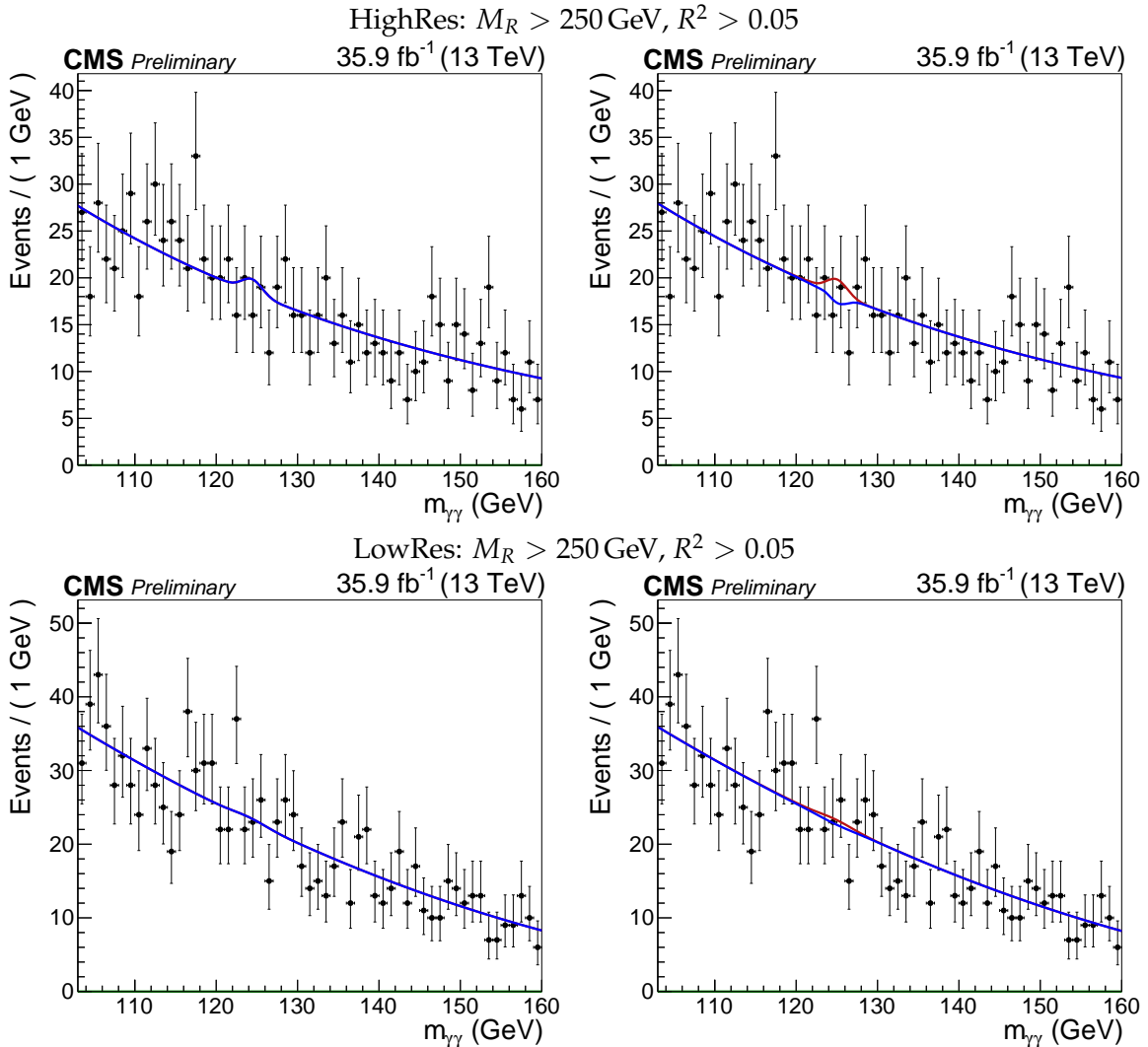


Figure 12: The diphoton mass distribution for the search region bin 11 are shown along with the background-only fit (left) and the signal plus background fit (right). The top row shows the HighRes category, while the bottom row shows the LowRes category. The red curve represents the background prediction; the green curve represents the signal; and the blue curve represents the sum of the signal and background. The definition of the bin is labeled above each pair of plots.

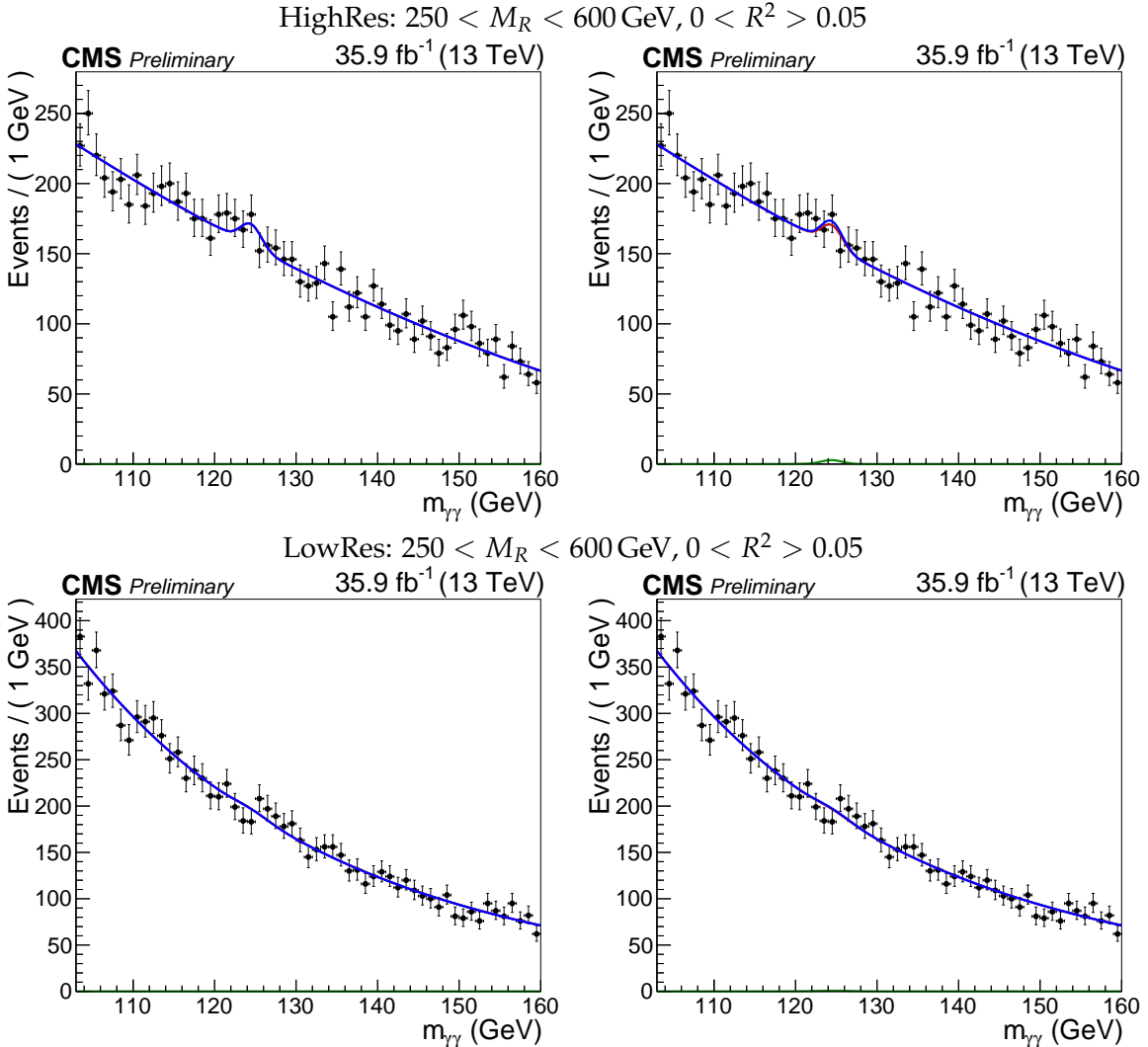


Figure 13: The diphoton mass distribution for the search region bin 12 are shown along with the background-only fit (left) and the signal plus background fit (right). The top row shows the HighRes category, while the bottom row shows the LowRes category. The red curve represents the background prediction; the green curve represents the signal; and the blue curve represents the sum of the signal and background. The definition of the bin is labeled above each pair of plots.

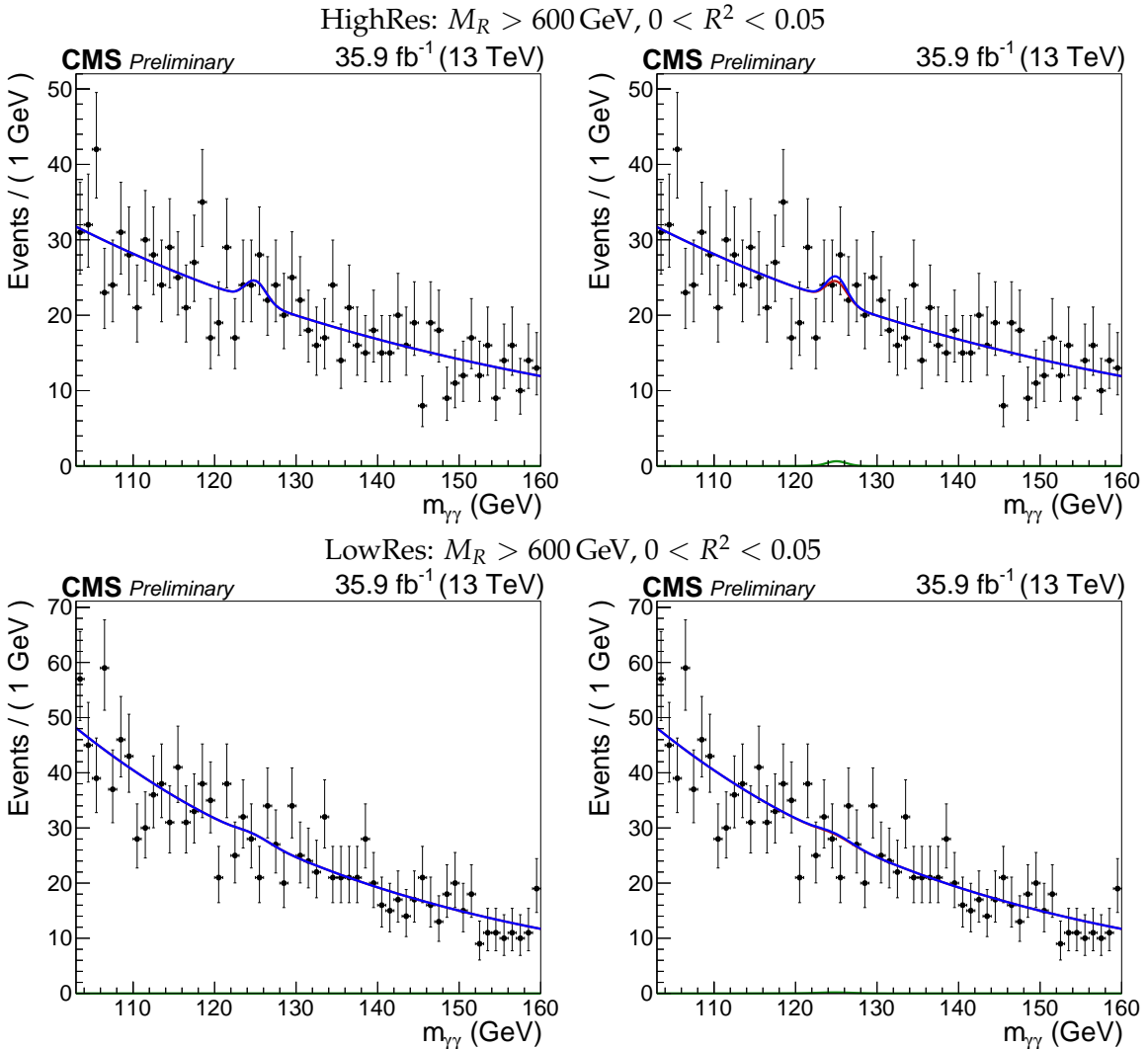


Figure 14: The diphoton mass distribution for the search region bin 13 are shown along with the background-only fit (left) and the signal plus background fit (right). The top row shows the HighRes category, while the bottom row shows the LowRes category. The red curve represents the background prediction; the green curve represents the signal; and the blue curve represents the sum of the signal and background. The definition of the bin is labeled above each pair of plots.